Quantum Hall effect in topological Dirac semimetals modulated by the Lifshitz transition of the Fermi arc surface states

Tao-Rui Qin,[1] Zhuo-Hua Chen [ORCID],[1] Tian-Xing Liu,[1] Fu-Yang Chen,[1] Hou-Jian Duan,[1,2]
Ming-Xun Deng [ORCID],[1,2,*] and Rui-Qiang Wang[1,2,†]

[1]*Guangdong Provincial Key Laboratory of Quantum Engineering and Quantum Materials, School of Physics,
South China Normal University, Guangzhou 510006, China*
[2]*Guangdong-Hong Kong Joint Laboratory of Quantum Matter, Frontier Research Institute for Physics,
South China Normal University, Guangzhou 510006, China*

We investigate the magnetotransport of topological Dirac semimetals (DSMs) while taking into account the Lifshitz transition of the Fermi arc surface states. We demonstrate that a bulk momentum-dependent gap term, which is usually neglected in the study of bulk energy-band topology, can cause the Lifshitz transition by developing an additional Dirac cone on the surface to prevent the Fermi arcs from connecting with the bulk Dirac points. As a result, Weyl orbits can be turned off by the surface Dirac cone without destroying the bulk Dirac points. In response to the surface Lifshitz transition, the Weyl-orbit mechanism for the three-dimensional (3D) quantum Hall effect (QHE) in topological DSMs will break down. The resulting quantized Hall plateaus can be thickness dependent, similar to those based on Weyl orbits but their widths and quantized values become irregular. Accordingly, we propose that apart from bulk Weyl nodes and Fermi arcs, surface Lifshitz transitions are also crucial for realizing stable Weyl orbits and 3D QHE in real materials.

I. INTRODUCTION

Topological semimetals are novel quantum states of matter in which the conduction and valence bands cross near the Fermi level at certain discrete momentum points or lines [1–10]. The gap-closing points or lines are protected by either crystalline symmetry or topological invariants [11,12]. A topological Dirac semimetal (DSM) hosts paired gap-closing points, referred to as Dirac points, which are stabilized by time-reversal, spatial-inversion, and crystalline symmetries. By breaking the time-reversal or spatial-inversion symmetry, a single Dirac point can split into a pair of Weyl nodes of opposite chiralities [13,14], leading to a topological transition from a Dirac to a Weyl semimetal [15–20]. Accompanied with the bulk topological transition, topological states protected by the quantized Chern flux will emerge on the surface to connect the split Weyl nodes, known as the Fermi arc surface states [7].

In topological DSMs, such as A_3Bi (A = Na,K,Rb) [4,5] and Cd_3As_2 [2,3], the Weyl nodes at the same Dirac point, belonging to different irreducible representations, cannot be coupled and have to seek a partner from the other Dirac point. As a consequence, the two Dirac points including two pairs of Weyl nodes are connected by two spin-polarized Fermi arcs [3–7]. The Fermi arc surface states are the most distinctive observable spectroscopic features of topological semimetals. However, their observation is sometimes limited by spectroscopic resolutions. Scientists have been searching for alternative smoking-gun features of topological semimetals, such as by means of transport phenomena [21–23]. Many interesting transport properties have been revealed in topological semimetals, including chiral-anomaly-induced negative magnetoresistance [24–30], Weyl-orbit-related quantum oscillations [31,32], Berry's phase π-related Aharonov-Bohm effect [33,34], bulk-surface interference-induced Fano effect [35], and topological pumping effect [36].

Recently, three-dimensional (3D) quantum Hall effect (QHE) because of the Fermi arcs was proposed in Weyl semimetals [10] and has led to an explosion of theoretical [37–50] and experimental [51–55] activities in the field of condensed matter physics. In a Weyl semimetal slab, the Weyl orbit which consists of Fermi arcs from opposite surfaces can support the electron cyclotron orbit for the QHE, making the 3D QHE available. The 3D QHE has been observed experimentally in topological DSMs [51–55] and the one from the Weyl-orbit mechanism is demonstrated to be thickness dependent [53]. However, for the topological DSMs, a single surface with two Fermi arcs can also support a complete Fermi loop required by the QHE, which can compete with the Weyl-orbit mechanism. The same-surface Fermi loop is not stable and can be deformed by bulk perturbations [12,56]. In real materials, the bulk perturbations are inevitable.

As we will show, when a bulk momentum-dependent gap term is included, Lifshitz transition can happen for the Fermi arc surface states, in which the double Fermi arcs on the DSM surface can be continuously deformed into a closed Fermi loop and separate from the bulk Dirac points. The Lifshitz transition involves a change of the Fermi surface topology

*dengmingxun@scnu.edu.cn
†wangruiqiang@m.scnu.edu.cn

125111-1

that is not connected with a change in the symmetry of the lattice [57–62]. Therefore, the Lifshitz transition can take place without destroying the topology of the bulk energy band. A natural question in this regard is how the deformation of the Fermi arcs influences the 3D QHE of topological DSMs, especially when the Fermi arcs, as key ingredients for the Weyl orbits, breaks free from the bulk Dirac points.

In this paper, we investigate the QHE in topological DSMs, taking into account the surface Lifshitz transition that can be modulated by a bulk momentum-dependent gap term. It is demonstrated that while the bulk Dirac points are robust against the momentum-dependent gap term, an additional two-dimensional (2D) Dirac cone can develop on the surface, which deforms the surface Fermi arcs from a curve to discrete points and further to a Fermi loop coexisting with the bulk Dirac points. During this process, the bulk topological properties remain unchanged but the Weyl orbits can be turned off. The joint effect of the Weyl orbits and surface Lifshitz transition makes the QHE quite complicated. We find that when the Weyl orbits are broken by the surface Dirac cone, the bulk and surface states can form Landau levels (LLs) and contribute independently to the QHE. The resulting Hall plateaus are sensitive to the thickness of the sample but their widths and quantized values are irregularly distributed. The rest of this paper is organized as follows. In Sec. II, we introduce the model Hamiltonian and bulk spectrum. The Lifshitz transition of the Fermi arcs and the LLs are analyzed in Sec. III and Sec. IV, respectively. The QHE is studied in Sec. V and the last section contains a short summary.

II. HAMILTONIAN AND BULK SPECTRUM

We begin with a low-energy effective Hamiltonian for the topological DSMs

$$\mathcal{H}(\boldsymbol{k}) = \varepsilon_{\boldsymbol{k}} + \lambda(k_x \sigma_z \tau_x - k_y \tau_y) + m_{\boldsymbol{k}} \tau_z + \Lambda(\boldsymbol{k}), \quad (1)$$

with $m_{\boldsymbol{k}} = m_0 - m_1 k_z^2 - m_2 k_\parallel^2$ and $\varepsilon_{\boldsymbol{k}} = c_0 + c_1 k_z^2 + c_2 k_\parallel^2$, where $k_\parallel = \sqrt{k_x^2 + k_y^2}$, and $\sigma_{x,y,z}$ ($\tau_{x,y,z}$) is the Pauli matrix acting on the spin (orbital parity) degree of freedom. This model has been widely adopted to capture the topological properties of topological DSMs Cd_3As_2 [3] and A $_3$Bi (A = Na, K, Rb) [4]. In the absence of $\Lambda(\boldsymbol{k})$, $[\sigma_z, \mathcal{H}(\boldsymbol{k})] = 0$ and the topological DSMs characterized by Hamiltonian Eq. (1) can be viewed as two superposed copies of a Weyl semimetal with two Weyl nodes, which possesses two sets of surface Fermi arcs in the surface Brillouin zone, as illustrated by Figs. 1(a)–1(b) and 1(e)–1(f). $\Lambda(\boldsymbol{k})$ can mix the eigenstates of opposite spins away from the Dirac points and plays the role of a momentum-dependent gap term whose form is determined by crystal symmetries.

Specifically, for a DSM with fourfold rotational symmetry, such as Cd_3As_2, the momentum-dependent gap term can take the form $\Lambda(\boldsymbol{k}) = \alpha k_z (k_+^2 \sigma_- + k_-^2 \sigma_+) \tau_x / 2$ with $k_\pm = k_x \pm i k_y$ and $\sigma_\pm = \sigma_x \pm i \sigma_y$. Diagonalizing Hamiltonian Eq. (1) yields the continuum bulk spectrum

$$E_\pm(\boldsymbol{k}) = \varepsilon_{\boldsymbol{k}} \pm \sqrt{\lambda^2 k_\parallel^2 + m_{\boldsymbol{k}}^2 + \alpha^2 k_\parallel^4 k_z^2}, \quad (2)$$

from which we can determine the energy location $E_D = c_0 + c_1 k_w^2$ and momentum locations $\boldsymbol{K}_\pm = (0, 0, \pm k_w)$ of the bulk
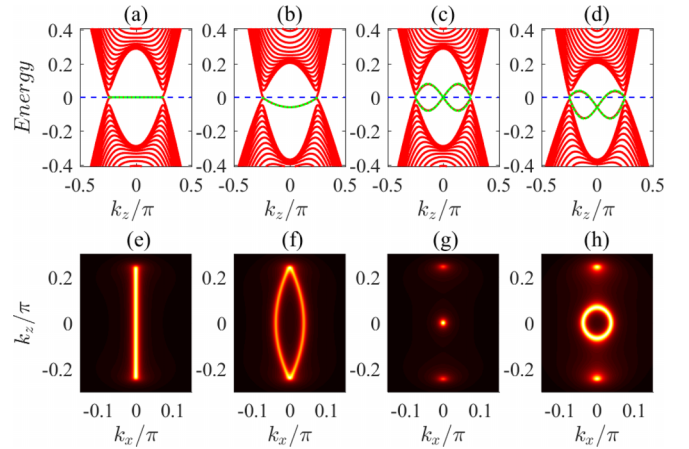

FIG. 1. (a)–(d) The dispersion (red) by diagonalizing Hamiltonian Eq. (12) for (a) $\alpha = 0$, $c_1 = c_2 = 0$, (b) $\alpha = 0$, $c_1 = 3c_2 = 0.15$, (c) $\alpha = 0.5$, $c_1 = c_2 = 0$, and (d) $\alpha = 0.5$, $c_1 = 3c_2 = 0.15$, with $k_x = 0$ and $E_D = 0$ denoted by the blue dashed lines. The green dotted curves are determined from Eq. (9), self-consistently. (e)–(h) The $\boldsymbol{k}$-resolved DOSs corresponding to (a)–(d) at $E_F = E_D$. The rest of the parameters are set as $\lambda = 0.5$, $k_w = \pi/4$, $m_0 = \pi^2/32$, $m_2 = 0.5$, and $N_y = 50$.

Dirac points with $k_w = \sqrt{m_0/m_1}$. As $\varepsilon_{\boldsymbol{k}}$ possesses the symmetries of $m_{\boldsymbol{k}}$, it does not qualitatively change the Dirac spectrum in the bulk, but introduces an asymmetry between the positive (electrons) and negative (holes) energy branches and, consequently, breaks the particle-hole symmetry. The electron-hole asymmetry will curve the Fermi arcs, which was demonstrated to be crucial for the LLs around the Weyl nodes [10]. While $\Lambda(\boldsymbol{k})$ can profoundly change the spectrum of quasiparticles for sufficiently large $k_\parallel$, it preserves all the symmetries of the crystal structure and vanishes at the Dirac points. Therefore, the bulk Dirac points are robust against $\Lambda(\boldsymbol{k})$, as seen from Eq. (2), where both momentum and energy locations of the Dirac points are regardless of α. For this reason, $\Lambda(\boldsymbol{k})$ is usually treated as a bulk perturbation that does not destroy the bulk topology.

For states near the bulk Dirac points, the quasiparticles can be described by linearizing Hamiltonian Eq. (1) around $\boldsymbol{K}_\pm$, such that $\Lambda(\boldsymbol{k})$ can be neglected. However, in a topological DSM slab, the Fermi arcs, which connect the bulk Dirac points separated far away in momentum space, can extend to large $\boldsymbol{k}$ where the spectrum can be dramatically modified by the momentum-dependent gap term. In the following, we elucidate that, in response to the momentum-dependent gap term, the surface states of topological DSMs will experience a Lifshitz transition, during which process the Fermi arcs can exist without connecting the bulk Dirac points.

III. LIFSHITZ TRANSITION OF THE FERMI ARCS

To better understand how the Fermi arc surface states evolve with the momentum-dependent gap term, we consider a topological DSM slab with open boundaries at $y = \pm L/2$ and derive the surface states for the xz plane. For such a finite-size system, k_y in Eq. (1) is no longer a good quantum number and should be replaced with the operator $-i\partial_y$. In

the spirit of perturbation theory, we construct an unperturbed surface basis using the surface wave functions without $\Lambda(\mathbf{k})$, and obtain the effective Hamiltonian for the surface states by projecting Eq. (1) onto this unperturbed surface basis. For ease of discussion, we assume $m_2 > |c_2|$ and select E_D as potential energy zero, i.e., $c_0 = -c_1 k_w$.

By setting $\alpha = 0$ and solving the differential equation $\mathcal{H}(k_x, -i\partial_y, k_z)\Psi_{k_x,k_z}(y) = E\Psi_{k_x,k_z}(y)$ with the open boundary conditions $\Psi_{k_x,k_z}(\pm L/2) = 0$, we can evaluate the unperturbed surface wave functions as $\Psi_{k_x,k_z}^{\beta,s}(y) = (\frac{1+s}{2}, \frac{1-s}{2})^T \otimes \Psi_\beta(y)$, which are spin resolved, with $s = \pm 1$ being the eigenvalue of σ_z and

$$\Psi_\beta(y) = \begin{pmatrix} \beta \cos\frac{\vartheta}{2} \\ -\sin\frac{\vartheta}{2} \end{pmatrix} \frac{e^{\kappa_-(\beta y-\frac{L}{2})} - e^{\kappa_+(\beta y-\frac{L}{2})}}{\sqrt{N_\beta}}. \tag{3}$$

Here, $\beta = \pm$ corresponds to the surface at $y = \pm L/2$, $N_\beta = \int_{-\frac{L}{2}}^{\frac{L}{2}} |e^{\kappa_-(\beta y-\frac{L}{2})} - e^{\kappa_+(\beta y-\frac{L}{2})}|^2 dy$ is the normalization coefficient, and

$$\vartheta = \tan^{-1}\left[\frac{2\lambda(m_2-c_2)(\kappa_+ + \kappa_-)}{\lambda^2 - (m_2-c_2)^2(\kappa_+ + \kappa_-)^2}\right]. \tag{4}$$

Here, $\kappa_\pm$ is a solution to $E_\pm(k_x, -i\kappa, k_z) = E$ reading

$$\kappa_\pm = \sqrt{k_x^2 + \frac{\zeta_\lambda \pm (\zeta_\lambda^2 - \zeta_+\zeta_-)^{1/2}}{m_2^2 - c_2^2}}, \tag{5}$$

with $\zeta_\lambda = \frac{\lambda^2 - \zeta_+ + \zeta_-}{2}$ and

$$\zeta_\pm = (m_2 \pm c_2)\left[(m_1 \mp c_1)(k_w^2 - k_z^2) \mp E\right]. \tag{6}$$

The surface states are confined within the region defined by $\mathrm{Re}(\kappa_\pm) > 0$. Subsequently, by performing the projection operation

$$\mathcal{H}_{\mathrm{surf}}^{\beta,ss'} = \langle \Psi_{k_x,k_z}^{\beta,s}(y)|\mathcal{H}(k_x, -i\partial_y, k_z)|\Psi_{k_x,k_z}^{\beta,s'}(y)\rangle, \tag{7}$$

we can obtain the effective surface Hamiltonian

$$\mathcal{H}_{\mathrm{surf}}^\beta(k_x, k_z) = \tilde{\varepsilon}_{\mathbf{k}} - \beta \sin\vartheta (\lambda k_x \sigma_z + \tilde{\alpha} k_z \sigma_x), \tag{8}$$

where $\tilde{\alpha} = \alpha(k_x^2 - \kappa_+\kappa_-)$, $\tilde{\varepsilon}_{\mathbf{k}} = \tilde{c}_1(k_z^2 - k_w^2) + \tilde{c}_2(k_x^2 + \kappa_+\kappa_-)$, and $\tilde{c}_l = c_l - m_l\cos\vartheta$ with $l = 1, 2$. The details can be found in Ref. [63].

As demonstrated by Eq. (8), the surface Hamiltonian displays a 2D Dirac structure with spin-momentum locking, resembling the surface states of 3D topological insulators. However, unlike the 3D topological insulators, the bulk spectrum here is also gapless, meaning that the surface Dirac point can coexist with the bulk Dirac points. By diagonalizing Eq. (8), we can obtain

$$E_\eta^\beta(k_x, k_z) = \tilde{\varepsilon}_{\mathbf{k}} - \eta\beta \sin\vartheta \sqrt{\lambda^2 k_x^2 + \tilde{\alpha}^2 k_z^2}, \tag{9}$$

where $\eta = \pm 1$ labels the conduction/valence band. It should be noted that because $\kappa_\pm$ is energy dependent, Eq. (9) is only a formal solution for the surface spectrum. The exact surface dispersion involves a self-consistent calculation of Eq. (9) by replacing $E \to E_\eta^\beta(k_x, k_z)$ in Eq. (6). The numerical results of the surface dispersion are presented by the green dotted curves in Figs. 1(a)–1(d).

In order to show the bulk states and surface Fermi arcs simultaneously, we evaluate the $\mathbf{k}$-resolved density of states (DOSs) for a given energy E through

$$\rho(E, k_x, k_z) = -\frac{1}{\pi}\mathrm{Im}\,\mathrm{Tr}\left(\frac{1}{E + i0^+ - H}\right), \tag{10}$$

in which $H = \sum_{\mathbf{k}} c_{\mathbf{k}}^\dagger \mathcal{H}_{\mathbf{k}}^{\mathrm{tb}} c_{\mathbf{k}}$ is the tight-binding Hamiltonian corresponding to Eq. (1). Here, $c_{\mathbf{k}}^\dagger$ ($c_{\mathbf{k}}$) is the fermion creation (annihilation) operator and

$$\mathcal{H}_{\mathbf{k}}^{\mathrm{tb}} = M_{\mathbf{k}} + \lambda(\sin k_x \sigma_z \tau_x - \sin k_y \tau_y) - 2\alpha \sin k_z$$
$$\times [(\cos k_x - \cos k_y)\sigma_x - \sin k_x \sin k_y \sigma_y]\tau_x \tag{11}$$

is the single-particle Hamiltonian obtained from Eq. (1) by the transforms $k_a \to \sin k_a$ and $k_a^2 \to 2 - 2\cos k_a$, with $a = x, y, z$, $M_{\mathbf{k}} = f_1(\cos k_z - \cos k_w) + f_2(\cos k_x + \cos k_y - 2)$, and $f_l = 2(m_l\tau_z - c_l)$. By performing the Fourier transform $c_{\mathbf{k}} \to \sum_n c_n e^{-ik_y y_n}$, we can discretize the tight-binding Hamiltonian as [63]

$$H = \sum_n c_n^\dagger h_0 c_n + \sum_n (c_n^\dagger h_y c_{n+1} + \mathrm{h.c.}), \tag{12}$$

where the hopping matrices are given by

$$h_0 = f_0 + f_1 \cos k_z + f_2 \cos k_x + f_x \sin k_x$$
$$- \alpha\sigma_x\tau_x[\sin(k_z + k_x) + \sin(k_z - k_x)], \tag{13}$$

$$h_y = \frac{f_2 + if_y}{2} + \alpha\sigma_x\tau_x \sin k_z$$
$$+ i\alpha\sigma_y\tau_x \frac{\cos(k_z + k_x) - \cos(k_z - k_x)}{2}, \tag{14}$$

with $f_0 = -2f_2 - f_1 \cos k_w$ and $f_{x(y)} = \lambda\sigma_{z(0)}\tau_{x(y)}$.

In Fig. 1, we plot the numerical spectrum and $\mathbf{k}$-resolved DOSs for Eq. (12). As shown by the green dotted curves in Figs. 1(a)–1(d), the self-consistent calculation of Eq. (9) aligns with the results obtained through numerical diagonalization of Eq. (12). As depicted in Figs. 1(a) and 1(e), the surface spectrums without $\varepsilon_{\mathbf{k}}$ and $\Lambda(\mathbf{k})$ are k_z independent and intersect at E_D with a quadruply degenerate line connecting the two Dirac points. The flat Fermi line can be easily modified by perturbations, which elucidates why particle-hole asymmetry and momentum-dependent gap terms are important to the surface states. A nonzero $\varepsilon_{\mathbf{k}}$ cannot gap the surface spectrum but will cause bending of the Fermi lines into a parabola, as shown by Fig. 1(b). Consequently, the Fermi arcs with opposite spin, due to the spin-dependent term in Eq. (8), will curve in opposite direction at the Fermi level, forming a closed loop with a discontinuous kink at the Dirac points, as indicated by Fig. 1(f).

By contrast, when the momentum-dependent gap term is included, the Fermi lines with opposite spin will repel each other and remove the spin degeneracy due to the noncommutation between σ_z and $\mathcal{H}_{\mathrm{surf}}^\beta(k_x, k_z)$. Since $\Lambda(\mathbf{k}) = 0$ for $k_\parallel = 0$ or $k_z = 0$, the surface spectrums keep crossing at $\mathbf{k} = 0$, $\mathbf{K}_\pm$, as shown by Fig. 1(c). Therefore, a 2D Dirac point develops on each surface, which coexists with the bulk Dirac points. The surface Dirac points, similar to the bulk Dirac points, are robust against $\Lambda(\mathbf{k})$, but differently, the energy location of the surface Dirac points can be modulated by the particle-hole

asymmetry. In the presence of particle-hole symmetry, i.e., $\varepsilon_{\boldsymbol{k}} = 0$, the energy location of the surface Dirac points is identical to the bulk Dirac points. Thus, at $E_F = E_D$, the Fermi line in Fig. 1(e) deforms into three Fermi points in Fig. 1(g). When particle-hole symmetry is broken by a finite $\varepsilon_{\boldsymbol{k}}$, the surface Dirac points will shift away from E_D, after that the surface Fermi point around $\boldsymbol{k} = 0$ turns to a Fermi loop, as demonstrated by Fig. 1(h), which prevents the Fermi arcs from connecting the bulk Dirac points.

Consequently, although the surface spectrums remain intersecting with the bulk Dirac points, the surface states will experience a Lifshitz transition with the Fermi arcs changing from a curve to discrete gap-closing points and further to a Fermi loop coexisting with the bulk Dirac points. Throughout this process, the Weyl orbits can be deactivated without compromising the topological properties of the bulk energy band.

IV. LLS AND PROBABILITY DENSITY DISTRIBUTION

Upon the application of an external magnetic field, a Peierls phase should be added to the hopping matrices as electrons jump from position $\boldsymbol{r}_n$ to $\boldsymbol{r}_m$, i.e., $t_{mn} \to t_{mn}e^{-i\varphi_{mn}}$ with $\varphi_{mn} = \frac{2\pi}{\Phi_0}\int_{\boldsymbol{r}_m}^{\boldsymbol{r}_n} \boldsymbol{A}\cdot d\boldsymbol{l}$ and $\Phi_0 = h/e$ being the unit-flux quantum. When the magnetic field is applied in the y direction, we can choose the Landau gauge $\boldsymbol{A} = (0, 0, -Bx)$. To include the magnetic field, we further discretize Eq. (12) in direction x as [63]

$$H = \sum_{mn} c_{m,n}^{\dagger}(T_m c_{m,n} + T_{m,x}c_{m+1,n} + T_{m,y}c_{m,n+1}$$
$$+ T_{m,\alpha}c_{m+1,n-1} - T_{m,\alpha}c_{m+1,n+1}) + h.c., \quad (15)$$

where the Fourier transform $c_n \to \sum_m c_{m,n}e^{-ik_x x_m}$ has been adopted and the hopping matrices are given by

$$T_m = \frac{f_0 + f_1 \cos\left(k_z - m/\ell_B^2\right)}{2}, \quad (16)$$

$$T_{m,\alpha} = \frac{\alpha}{2}\sigma_y\tau_x \sin\left(k_z - \frac{m+1/2}{\ell_B^2}\right), \quad (17)$$

$$T_{m,y} = \frac{f_2 + if_y}{2} + \alpha\sigma_x\tau_x \sin\left(k_z - m/\ell_B^2\right), \quad (18)$$

$$T_{m,x} = \frac{f_2 - if_x}{2} - \alpha\sigma_x\tau_x \sin\left(k_z - \frac{m+1/2}{\ell_B^2}\right), \quad (19)$$

with $\ell_B = \sqrt{\hbar/(eB)}$ being the magnetic length.

After introducing the magnetic field, we continue to demonstrate the relation between Eq. (11) and Eq. (15). By performing an inverse Fourier transform on Eq. (15), we can derive

$$\tilde{\mathcal{H}}_{\boldsymbol{k}} = f_1(\cos\kappa_z - \cos k_w) + f_2(\cos k_x + \cos k_y - 2)$$
$$+ \lambda(\sin k_x \tau_x\sigma_z - \sin k_y \tau_y) - \alpha\tau_x\left[\left(\frac{\sin\kappa_z^+ - \sin\kappa_z^-}{2}\right.\right.$$
$$\left.- \cos k_y \sin\kappa_z\right)\sigma_x - \sin k_y \frac{\cos\kappa_z^+ - \cos\kappa_z^-}{2}\sigma_y\right], \quad (20)$$

with $\kappa_z = k_z - x/\ell_B^2$ and $\kappa_z^{\pm} = \pm\kappa_z + k_x$. Here, we have used the Baker-Campbell-Hausdorff formula, i.e., $e^{\hat{A}+\hat{B}} = e^{\hat{A}}e^{\hat{B}}e^{-\frac{1}{2}[\hat{A},\hat{B}]}$. It is clear that $\tilde{\mathcal{H}}_{\boldsymbol{k}} = \mathcal{H}_{\boldsymbol{k}\to\boldsymbol{k}+e\boldsymbol{A}/\hbar}^{\text{tb}}$ follows the
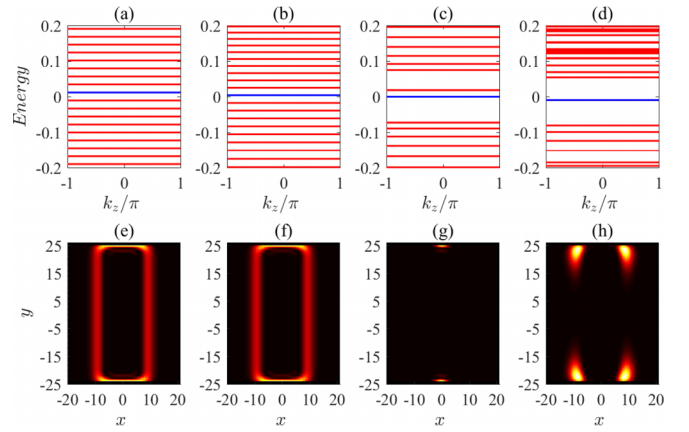

FIG. 2. The LLs for (a) $\alpha = 0$, $c_1 = c_2 = 0$, (b) $\alpha = 0$, $c_1 = 3c_2 = 0.15$, (c) $\alpha = 0.5$, $c_1 = c_2 = 0$, and (d) $\alpha = 0.5$, $c_1 = 3c_2 = 0.15$. (e)–(h) The probability density $|\psi_{k_z,\mu}|^2$ for the blue LLs in (a)–(d), in which $\psi_{k_z,\mu}$ is the μth LL's wavefunction. Here, we set $2\pi\ell_B^2 = N_x$, $k_z = \pi$, $k_w = \pi/2$, $N_x = 40$ and other parameters the same as Fig. 1.

Peierls substitution. However, for $\alpha \neq 0$, one should be very careful when using direct Peierls substitution because of the cross-momentum term in $\Lambda(\boldsymbol{k})$. For example, as we transform Eq. (20) to the lattice form for numerical calculation, there will emerge an additional phase $\ell_B^{-2}/2$ such as in Eqs. (17) and (19). The underlying physics for the additional phase is that after Peierls substitution, different momentum components can be noncommutative, e.g., $[k_x, \kappa_z] = i\ell_B^{-2}$, and the Baker-Campbell-Hausdorff formula must be adopted. For instance, when transforming Eq. (12) to Eq. (15), one should express the trigonometric functions in the exponential form and then introduce Peierls phase via the transforms $e^{ik_z} \to e^{i\kappa_z}$ and $e^{i(k_x\pm k_z)} \to e^{i\kappa_z^{\pm}} = e^{\pm i(\kappa_z - \ell_B^{-2}/2)}e^{ik_x}$.

By numerically diagonalizing Hamiltonian Eq. (15), we can obtain the LLs and spatial distribution of the electron probability density, as shown in Fig. 2. Through analyzing the spatial distribution of the probability density, we can easily determine whether or not the LLs are formed by the Weyl orbits. From Figs. 2(a) and 2(e), it is evident that the LLs can be formed from the Weyl-orbit mechanism, even when there is no curvature in the Fermi arcs. In the Weyl-orbit mechanism, the surface fermions driven by the magnetic field will move along the Fermi arcs from one Dirac valley to the other and tunnel to opposite surfaces at Dirac points via bulk states. As a result, the probability density exhibits a closed loop with two bright stripes crossing the bulk and connecting the surface states, observed in Fig. 2(e). The width of the bright stripes $\sim 2\ell_B$ corresponds to the cyclotron radius of the bulk Dirac fermions, while their separation encodes the momentum distance between the Dirac points. The cyclotron center $x_c = \ell_B^2 k_z$ of the fermions in different Dirac valleys differs by $\Delta x_c = 2\ell_B^2 k_w$, which is exactly the distance between the two bright stripes.

A finite $\varepsilon_{\boldsymbol{k}}$ that curves the Fermi arcs in the surface Brillouin zone will shift the LLs integrally by modifying the magnetic flux enclosed by the Weyl orbits, as demonstrated by Figs. 2(b) and 2(f). In this case, the Weyl orbits will not be destroyed, so the LLs remain evenly spaced. As expected,
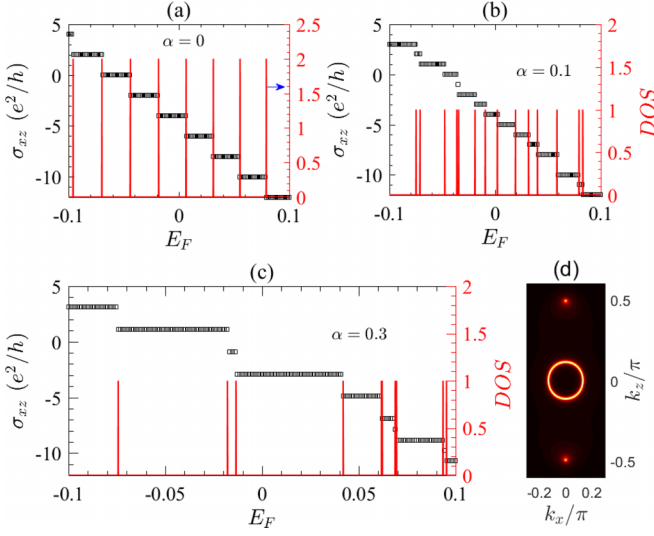
FIG. 3. The Hall conductivity (left axis) and DOS (right axis) for a given k_z with (a) $\alpha = 0$, (b) $\alpha = 0.1$, and (c) $\alpha = 0.3$. (d) The Fermi surface for $E_F = 0$ and $\alpha = 0.3$ in the absence of magnetic field. The parameters are the same as Fig. 2.

the LLs will respond dramatically to $\Lambda(\mathbf{k})$, as seen from Figs. 2(c) and 2(d), where the LLs are irregularly distributed due to turning off of the Weyl-orbit mechanism by the surface Dirac cone. The probability densities displayed in Figs. 2(g) and 2(h), as well as Fig. 4(c), illustrate that the bulk and surface states can support the cyclotron orbit and form the
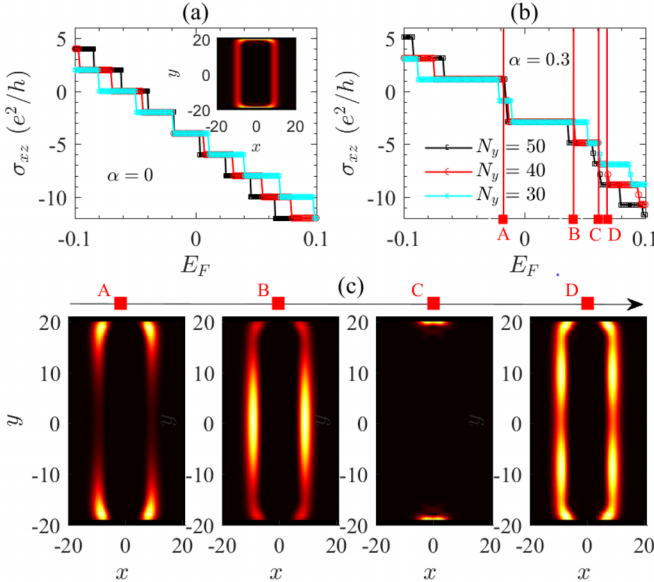

FIG. 4. (a)–(b) Evolution of the Hall conductivity with the sample thickness, i.e., $N_y = (30, 40, 50)$, for (a) $\alpha = 0$ with the inset showing that the LLs are from the Weyl-orbit mechanism, and (b) $\alpha = 0.3$ with the red lines marked by A–D denoting the LLs for $N_y = 40$. (c) The probability density of the LLs marked in (b), which indicates that the surface and bulk states are disconnected, i.e., the Weyl orbits have been turned off. The parameters are chosen the same as Fig. 3.

LLs, independently. The complicated LLs in Figs. 2(c) and 2(d) are results of the superposition of bulk and surface LLs.

The surface LLs are similar to those on the surfaces of 3D topological insulators, as implied by the surface effective Hamiltonian. However, since the effective Fermi velocity $\tilde{\alpha}$ in Eq. (8) depends on momentum, the surface LLs are more complicated compared to those observed on the surfaces of 3D topological insulators. For finite Fermi energies, the closed bulk Fermi surface in each Dirac valley can form a cyclotron orbit, giving rise to the bulk LLs. Without boundaries, the bulk LLs disperse along the magnetic field direction and prevent the quantization of the Hall conductivity. Here, due to the open boundaries, the Dirac fermions are confined in the y direction, and as a result, these bulk LLs become discretized, similar to a one-dimensional infinite potential well. The quantized levels are not evenly spaced, and as demonstrated below, the bulk LLs will contribute to irregular QHE.

V. EVOLUTION OF THE QHE WITH THE SURFACE LIFSHITZ TRANSITION

As discussed above, in the presence of the momentum-dependent gap term, the Weyl orbit near the Dirac points will disappear. However, the LLs remain discrete, indicating that the QHE can occur in topological DSMs without involving the Weyl-orbit mechanism. Since k_z is a good quantum number, we can calculate the Hall conductivity using the Kubo formula [10,37–40]

$$\sigma_{xz} = \frac{i\hbar e^2}{L_x L_z} \sum_{k_z, \mu \neq \nu} \left(f_{\nu, k_z} - f_{\mu, k_z} \right)$$

$$\times \frac{\langle \psi_{k_z, \mu} | \hat{v}_x | \psi_{k_z, \nu} \rangle \langle \psi_{k_z, \nu} | \hat{v}_z | \psi_{k_z, \mu} \rangle}{\left(\varepsilon_{k_z, \mu} - \varepsilon_{k_z, \nu} \right)^2}, \quad (21)$$

where ε_{μ, k_z} denote respectively the μth energy of Eq. (15), and the velocity operators are defined as $\hat{v}_x = i\hbar^{-1} \sum_{mn} [H, c_{m,n}^\dagger x_m c_{m,n}]$ and $\hat{v}_z = \partial H / (\hbar \partial k_z)$. Here, $f_{\mu, k_z} = [1 + \exp(\frac{\varepsilon_{\mu, k_z} - E_F}{k_B T})]^{-1}$ is the Fermi-Dirac distribution function, with k_B and T being the Boltzmann's constant and temperature, respectively.

In Fig. 3, we present the numerical results for the Hall conductivity near the bulk Dirac points. As can be seen, the Hall conductivity exhibits a step-wise structure and jumps whenever the Fermi level crosses a LL. The Hall plateaus for $\alpha = 0$ are quantized as $2ne^2/h$, with n being an integer and the factor 2 owing to the spin degeneracy of the LLs. The spin degeneracy of the LLs can be characterized by the k_z-resolved DOS plotted on the right axis of Fig. 3. In the absence of the momentum-dependent gap term, the LLs are evenly spaced and therefore, all Hall plateaus have identical widths, as shown in Fig. 3(a). With increasing α, the Weyl orbits near the bulk Dirac points will be broken gradually, and as a result, the LLs become complicated and the widths of the Hall plateaus turn to be irregular, as observed in Figs. 3(b) and 3(c). With the Weyl orbits destroyed, the spin degeneracy of the LLs will be removed, leading to the emergence of odd Hall plateaus in Figs. 3(b) and 3(c).

The thickness dependence of the quantized Hall plateaus is one of the characteristic signals for 3D QHE [53]. The

Weyl-orbit-mediated 3D QHE is dependent on thickness, as shown in Fig. 4(a), where the width of the Hall plateaus increases as N_y decreases. However, from Fig. 4(b), we see that even when the Weyl orbits are turned off by the surface Dirac cone, the Hall plateaus can still be sensitive to sample thickness. The thickness-dependent QHE in the absence of Weyl orbits can be attributed to the bulk LLs, as a result of the energy quantization due to confinement in direction y, as illustrated by Fig. 4(c), where the probability density exhibits a standing-wave configuration. In contrast to the bulk LLs, the surface LLs are less sensitive to the thickness, as shown by the LL marked by C in Fig. 4(b). While the surface LLs are independent of thickness, the Hall plateau close to them can display thickness dependence because the surface LLs are surrounded by bulk LLs. We estimate the impact of disorder on the QHE in Fig. 5. It is evident that disorder will broaden the LLs, and as a result, the narrow Hall plateaus are heavily destroyed, while the wider ones remain relatively robust against disorder.

VI. CONCLUSION

In summary, we have investigated the QHE in topological DSMs, taking into consideration the surface Lifshitz transition modulated by a bulk momentum-dependent gap term. It is found that the bulk momentum-dependent gap term, as a higher-order momentum term, can be neglected when studying the bulk topological properties. However, it significantly deforms the Fermi arcs and leads to the surface Lifshitz transition. During the surface Lifshitz transition, a 2D Dirac cone develops for the surface states, which prevents the Fermi arcs from connecting the bulk Dirac points. As a result, the Weyl orbits can be turned off without breaking the topology of the bulk energy band. In response to the Lifshitz transition, the 3D QHE, because of the Weyl orbits, will break down, along with that the quantized Hall plateaus turn to be irregular. As a
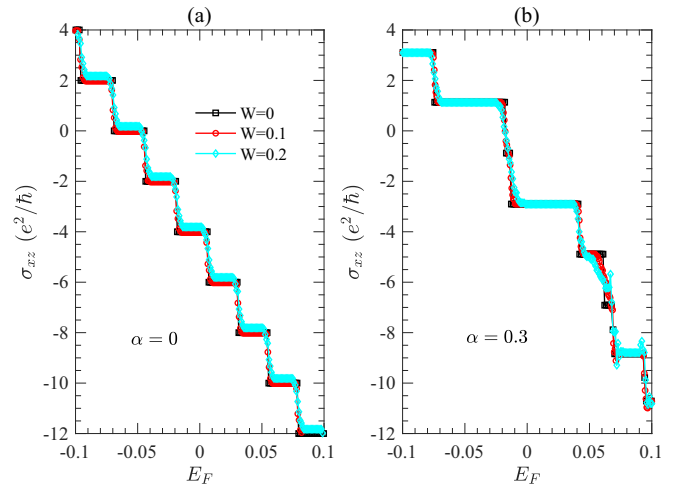

FIG. 5. Impact of Anderson disorder on the 3D QHE with the disorder strength $W = (0, 0.1, 0.2)$ for (a) $\alpha = 0$ and (b) $\alpha = 0.3$. Other parameters are the same as Fig. 4(c).

bulk perturbation, the momentum-dependent gap term is quite common in real materials. The Lifshitz transition of surface states also plays an important role in realizing stable Weyl orbits alongside bulk Weyl nodes and surface Fermi arcs.

[1] N. P. Armitage, E. J. Mele, and A. Vishwanath, Rev. Mod. Phys. **90**, 015001 (2018).

[2] M. Neupane, S.-Y. Xu, R. Sankar, N. Alidoust, G. Bian, C. Liu, I. Belopolski, T.-R. Chang, H.-T. Jeng, H. Lin, A. Bansil, F. Chou, and M. Z. Hasan, Nat. Commun. **5**, 3786 (2014).

[3] Z. Wang, H. Weng, Q. Wu, X. Dai, and Z. Fang, Phys. Rev. B **88**, 125427 (2013).

[4] Z. Wang, Y. Sun, X.-Q. Chen, C. Franchini, G. Xu, H. Weng, X. Dai, and Z. Fang, Phys. Rev. B **85**, 195320 (2012).

[5] Z. K. Liu, B. Zhou, Y. Zhang, Z. J. Wang, H. M. Weng, D. Prabhakaran, S.-K. Mo, Z. X. Shen, Z. Fang, X. Dai, Z. Hussain, and Y. L. Chen, Science **343**, 864 (2014).

[6] B.-J. Yang and N. Nagaosa, Nat. Commun. **5**, 4898 (2014).

[7] X. Wan, A. M. Turner, A. Vishwanath, and S. Y. Savrasov, Phys. Rev. B **83**, 205101 (2011).

[8] C.-L. Zhang, S.-Y. Xu, I. Belopolski, Z. Yuan, Z. Lin, B. Tong, G. Bian, N. Alidoust, C.-C. Lee, S.-M. Huang, T.-R. Chang, G. Chang, C.-H. Hsu, H.-T. Jeng, M. Neupane, D. S. Sanchez, H. Zheng, J. Wang, H. Lin, C. Zhang *et al.*, Nat. Commun. **7**, 10735 (2016).

[9] C. Zhang, E. Zhang, W. Wang, Y. Liu, Z.-G. Chen, S. Lu, S. Liang, J. Cao, X. Yuan, L. Tang, Q. Li, C. Zhou, T. Gu, Y. Wu, J. Zou, and F. Xiu, Nat. Commun. **8**, 13741 (2017).

[10] C. M. Wang, H.-P. Sun, H.-Z. Lu, and X. C. Xie, Phys. Rev. Lett. **119**, 136806 (2017).

[11] E. V. Gorbar, V. A. Miransky, I. A. Shovkovy, and P. O. Sukhachov, Phys. Rev. B **91**, 121101(R) (2015).

[12] M. Kargarian, M. Randeria, and Y.-M. Lu, Proc. Natl. Acad. Sci. USA **113**, 8648 (2016).

[13] H. Nielsen and M. Ninomiya, Phys. Lett. B **130**, 389 (1983).

[14] G. E. Volovik, *The Universe in a Helium Droplet*, Vol. 117 (Oxford University Press on Demand, 2003).

[15] S. Raza, A. Sirota, and J. C. Y. Teo, Phys. Rev. X **9**, 011039 (2019).

[16] A. A. Zyuzin, S. Wu, and A. A. Burkov, Phys. Rev. B **85**, 165110 (2012).

[17] P. Goswami and S. Tewari, Phys. Rev. B **88**, 245107 (2013).

[18] S. Han, G. Y. Cho, and E.-G. Moon, Phys. Rev. B **98**, 085149 (2018).

[19] M.-X. Deng, W. Luo, R.-Q. Wang, L. Sheng, and D. Y. Xing, Phys. Rev. B **96**, 155141 (2017).

[20] C. Chen, Z.-M. Yu, S. Li, Z. Chen, X.-L. Sheng, and S. A. Yang, Phys. Rev. B **99**, 075131 (2019).

[21] M. N. Ali, J. Xiong, S. Flynn, J. Tao, Q. D. Gibson, L. M. Schoop, T. Liang, N. Haldolaarachchige, M. Hirschberger, N. Ong, and R. Cava, Nature (London) **514**, 205 (2014).

[22] C. Shekhar, A. K. Nayak, Y. Sun, M. Schmidt, M. Nicklas, I. Leermakers, U. Zeitler, Y. Skourski, J. Wosnitza, Z. Liu, Y. Chen, W. Schnelle, H. Borrmann, Y. Grin, C. Felser, and B. Yan, Nat. Phys. **11**, 645 (2015).

[23] S. A. Parameswaran, T. Grover, D. A. Abanin, D. A. Pesin, and A. Vishwanath, Phys. Rev. X **4**, 031035 (2014).

[24] J. Xiong, S. K. Kushwaha, T. Liang, J. W. Krizan, M. Hirschberger, W. Wang, R. J. Cava, and N. P. Ong, Science **350**, 413 (2015).

[25] C.-Z. Li, L.-X. Wang, H. Liu, J. Wang, Z.-M. Liao, and D.-P. Yu, Nat. Commun. **6**, 10137 (2015).

[26] M.-X. Deng, G. Y. Qi, R. Ma, R. Shen, R.-Q. Wang, L. Sheng, and D. Y. Xing, Phys. Rev. Lett. **122**, 036601 (2019).

[27] M.-X. Deng, H.-J. Duan, W. Luo, W. Y. Deng, R.-Q. Wang, and L. Sheng, Phys. Rev. B **99**, 165146 (2019).

[28] S. Das, K. Das, and A. Agarwal, Phys. Rev. B **108**, 045405 (2023).

[29] S. Das, K. Das, and A. Agarwal, Phys. Rev. B **105**, 235408 (2022).

[30] K. Das, S. K. Singh, and A. Agarwal, Phys. Rev. Res. **2**, 033511 (2020).

[31] A. C. Potter, I. Kimchi, and A. Vishwanath, Nat. Commun. **5**, 5161 (2014).

[32] P. J. W. Moll, N. L. Nair, T. Helm, A. C. Potter, I. Kimchi, A. Vishwanath, and J. G. Analytis, Nature (London) **535**, 266 (2016).

[33] B.-C. Lin, S. Wang, L.-X. Wang, C.-Z. Li, J.-G. Li, D. Yu, and Z.-M. Liao, Phys. Rev. B **95**, 235436 (2017).

[34] L.-X. Wang, C.-Z. Li, D.-P. Yu, and Z.-M. Liao, Nat. Commun. **7**, 10769 (2016).

[35] S. Wang, B.-C. Lin, W.-Z. Zheng, D. Yu, and Z.-M. Liao, Phys. Rev. Lett. **120**, 257701 (2018).

[36] M.-X. Deng, Y.-C. Hu, W. Luo, H.-J. Duan, and R.-Q. Wang, Phys. Rev. B **106**, 075139 (2022).

[37] H. Li, H. Liu, H. Jiang, and X. C. Xie, Phys. Rev. Lett. **125**, 036602 (2020).

[38] R. Ma, D. N. Sheng, and L. Sheng, Phys. Rev. B **104**, 075425 (2021).

[39] H. Geng, G. Y. Qi, L. Sheng, W. Chen, and D. Y. Xing, Phys. Rev. B **104**, 205305 (2021).

[40] M. Chang, H. Geng, L. Sheng, and D. Y. Xing, Phys. Rev. B **103**, 245434 (2021).

[41] M. Chang and L. Sheng, Phys. Rev. B **103**, 245409 (2021).

[42] H.-Z. Lu, Natl. Sci. Rev. **6**, 208 (2019).

[43] S. Li, C. Wang, Z. Du, F. Qin, H.-Z. Lu, and X. Xie, npj Quantum Mater. **6**, 96 (2021).

[44] F. Qin, S. Li, Z. Z. Du, C. M. Wang, W. Zhang, D. Yu, H.-Z. Lu, and X. C. Xie, Phys. Rev. Lett. **125**, 206601 (2020).

[45] J. Gooth, S. Galeski, and T. Meng, Rep. Prog. Phys. **86**, 044501 (2023).

[46] Y.-X. Wang and Z. Cai, Phys. Rev. B **107**, 125203 (2023).

[47] Z. Du, C. Wang, H.-P. Sun, H.-Z. Lu, and X. Xie, Nat. Commun. **12**, 5038 (2021).

[48] X.-X. Zhang and N. Nagaosa, Nano Lett. **22**, 3033 (2022).

[49] R. Chen, T. Liu, C. M. Wang, H.-Z. Lu, and X. C. Xie, Phys. Rev. Lett. **127**, 066801 (2021).

[50] R. Chen, C. M. Wang, T. Liu, H.-Z. Lu, and X. C. Xie, Phys. Rev. Res. **3**, 033227 (2021).

[51] M. Uchida, Y. Nakazawa, S. Nishihaya, K. Akiba, M. Kriener, Y. Kozuka, A. Miyake, Y. Taguchi, M. Tokunaga, N. Nagaosa *et al.*, Nat. Commun. **8**, 2274 (2017).

[52] T. Schumann, L. Galletti, D. A. Kealhofer, H. Kim, M. Goyal, and S. Stemmer, Phys. Rev. Lett. **120**, 016801 (2018).

[53] C. Zhang, Y. Zhang, X. Yuan, S. Lu, J. Zhang, A. Narayan, Y. Liu, H. Zhang, Z. Ni, R. Liu *et al.*, Nature (London) **565**, 331 (2019).

[54] F. Tang, Y. Ren, P. Wang, R. Zhong, J. Schneeloch, S. A. Yang, K. Yang, P. A. Lee, G. Gu, Z. Qiao *et al.*, Nature (London) **569**, 537 (2019).

[55] B.-C. Lin, S. Wang, S. Wiedmann, J.-M. Lu, W.-Z. Zheng, D. Yu, and Z.-M. Liao, Phys. Rev. Lett. **122**, 036602 (2019).

[56] Z. Yan, Z. Wu, and W. Huang, Phys. Rev. Lett. **124**, 257001 (2020).

[57] I. Lifshitz, Sov. Phys. JETP **11**, 1130 (1960).

[58] Y. Okada, M. Serbyn, H. Lin, D. Walkup, W. Zhou, C. Dhital, M. Neupane, S. Xu, Y. J. Wang, R. Sankar, F. Chou, A. Bansil, M. Z. Hasan, S. D. Wilson, L. Fu, and V. Madhavan, Science **341**, 1496 (2013).

[59] I. Zeljkovic, Y. Okada, C.-Y. Huang, R. Sankar, D. Walkup, W. Zhou, M. Serbyn, F. Chou, W.-F. Tsai, H. Lin, A. Bansil, L. Fu, M. Z. Hasan, and V. Madhavan, Nat. Phys. **10**, 572 (2014).

[60] Y. Wu, N. H. Jo, M. Ochi, L. Huang, D. Mou, S. L. Bud'ko, P. C. Canfield, N. Trivedi, R. Arita, and A. Kaminski, Phys. Rev. Lett. **115**, 166602 (2015).

[61] K.-H. Ding, Z.-G. Zhu, Y.-L. Hu, and G. Su, Phys. Rev. B **104**, 155135 (2021).

[62] Y. Zheng, W. Chen, X. Wan, and D. Y. Xing, Chin. Phys. Lett. **40**, 097301 (2023).

[63] See the Supplemental Material at http://link.aps.org/supplemental/10.1103/PhysRevB.109.125111 for a detail derivation of the effective surface Hamiltonian and the tight-binding Hamiltonian.